

Phantom chain simulations for fracture of star polymer networks on the effect of arm molecular weight

Yuichi Masubuchi

Department of Materials Physics, Nagoya University

Nagoya 4648603, JAPAN

mas@mp.pse.nagoya-u.ac.jp

Ver. Aug 29, 2024

ABSTRACT

Despite many efforts, the fracture of network polymers under extension is yet to be elucidated. This study investigated the effect of strand molecular weight on the fracture characteristics of the networks made from star-branched prepolymers with various node functionalities $3 \leq f \leq 8$ and conversion ratios $0.6 \leq \varphi_c \leq 0.95$ via molecular simulations with phantom chains. The networks were created via end-linking reactions of star polymers with the arm molecular weight $N_a = 2, 5, \text{ and } 10$, simulated by a Brownian dynamics scheme. The cycle rank of the percolated network ξ was entirely consistent with the mean-field theory, implying that the reaction occurred independently and the network connectivity was statistically fair. Afterward, the networks were alternatively subjected to energy minimization and uniaxial stretch until the break. From the stress-strain curves recorded during the stretch, the stretch and stress at the break, λ_b and σ_b , and work for fracture W_b were obtained. For these values, the following relations were found: $\lambda_b \sim N_a^{1/2} \xi^{-1/3}$, $\sigma_b \sim v_{br} N_a^{4/3} \xi^{2/3}$, and $W_b \sim v_{br} N_a^{4/3} \xi^{2/3}$, where v_{br} is the branch point density.

KEYWORDS: coarse-grained simulations; mechanical properties; gels; rubbers;

INTRODUCTION

While the fracture of network polymers has been extensively studied, the fundamental mechanism remains unrevealed¹. According to earlier studies^{2,3}, the maximum stretch of a single strand determines the strain at the break of the network. Namely, the maximum stretch λ_{max} is written as $\lambda_{max} \sim L/R_0 \sim N^{1/2}$, where L and R_0 are the contour length and equilibrium end-to-end distance of the strand, and N is the number of Kuhn segments of the strand. This idea implicitly assumes that the broken strand is included in an aligned path to the elongational direction and that the path comprises only mechanically effective strands. Some simulation studies support these assumptions^{4,5}.

Meanwhile, some experiments reported interesting results that seem inconsistent with the theory. Akagi et al.⁶ determined λ_{max} for tetra-PEG gels with various prepolymer molecular weights (which correspond to N) and the conversion ratios φ_c by applying an extended Gent model⁷ to the stress-strain curves. They obtained an empirical relation written as $\lambda_{max} \sim N^{2/3}$. Fujiyabu et al.⁸ rationalized this formula, assuming that prepolymers are in a random, close-packed arrangement, and the strand length before stretch R_0 differs from the unperturbed dimension of the single prepolymer. They also demonstrated that the results from both tetra and tri-branch networks exhibit the same scaling concerning the relation between λ_{max} and N .

It should be noted that the experiments mentioned above did not measure the stretch at the breaking point. Experimentally evaluating network rupture is challenging due to the significant impact of defects at various length scales on the results; thus, few reports can be found on direct measurement of stretch at break for gels and rubbers. Nevertheless, λ_{max} obtained from stretch non-linearity may not coincide with stretch at the break because λ_{max} corresponds to the average stretch, and the breakage of a small number of strands triggers network rupture.

In this study, the effects of N on the network rupture were systematically investigated for star polymer networks with various node functionalities and conversion ratios through phantom chain network simulations. According to earlier studies⁹⁻¹³, the fracture characteristics, including strain and stress at break and work for fracture, were summarized as functions of cycle rank. The N -dependence of such functions was discussed, and the result implies that stretch at break depends

on $N^{1/2}$. Besides, strain at break and work for fracture depends on $N^{1/3}$. Details are shown below.

MODEL AND SIMULATIONS

Because the model and simulation method are the same as those reported earlier¹⁴, only a brief description is given below, with a set of typical snapshots and resultant mechanical behavior shown in Fig 1. Star-branch bead-spring chains replaced prepolymers. See Fig 1 (a) for the case of the bead number per arm $N_a = 2$ and the functionality $f = 4$. There is no interaction between beads except for the connectivity; thus, the chains can cross. These phantom chains were dispersed in a simulation box with periodic boundary conditions and equilibrated by the Brownian dynamics scheme. The equation of motion for the position of bead \mathbf{R}_i is as follows.

$$\mathbf{0} = -\zeta \dot{\mathbf{R}}_i + \frac{3k_B T}{a^2} \sum_k f_{ik} \mathbf{b}_{ik} + \mathbf{F}_i \quad (1)$$

The first term on the right-hand side is the drag force, and ζ is the friction coefficient. The second term is the balance of tension among connected bonds. a is the average length under equilibrium for the bond vector $\mathbf{b}_{ik} \equiv \mathbf{R}_i - \mathbf{R}_k$, k_B is the Boltzmann constant, and T is the temperature. f_{ik} is the non-linear spring coefficient written as $f_{ik} = (1 - \mathbf{b}_{ik}^2/b_{\max}^2)^{-1}$ with the maximum stretch b_{\max} . This finite extensibility was employed to avoid excessive thermal elongations of the bonds. After sufficient equilibration, gelation via end-linking reactions was simulated^{15,16}. According to the experimental setup, the prepolymers were colored in two different chemistries (red and blue), and the reaction occurred only between other colors to eliminate the formation of primary loops. Figure 1 (b) exhibits an example of gels with the conversion ratio, φ_c , at 0.95, the ratio of reacted arms to all the arms in the system. In a similar manner to earlier studies¹⁷⁻²⁰, energy minimization was applied to the obtained network without Brownian motion for the total bond energy written below.

$$U = -\frac{3k_B T b_{\max}^2}{2a^2} \sum_{i,k} \ln \left(1 - \frac{\mathbf{b}_{ik}^2}{b_{\max}^2} \right) \quad (2)$$

Note that this energy exclusively comes from the non-linear spring constant f_{ik} employed in the Brownian scheme since no inter-bead interaction is considered. The energy-minimized network is shown in Fig 1 (c). Such a network was elongated quasi-statically by alternative application of affine elongation with an infinitesimal strain $\Delta\varepsilon$ and energy-minimization, as shown in Figs 1

(d)-(e). During the elongation, bonds are removed when they exceed a specific maximum value, b_c . See Fig 1 (j), where a decrease of φ_c is initiated around the applied (true) strain ε around unity due to the bond breakage. The simulation continued until the network percolation was eliminated to the elongated direction, as seen in Figs 1 (f)-(h). The dispersed dots in Fig 1 (h) are isolated small clusters where the bond length becomes zero due to energy minimization. Elongational (true) stress σ was recorded as a function of ε , as demonstrated in Fig 1 (i), and strain and stress at break, ε_b and σ_b , were obtained from such a plot. Work for fracture W_b was calculated by numerically integrating the stress-strain relation until the network breaks. The employed quasi-static scheme avoids the effects of stretch rate, neglecting structural relaxations after every bond scission²¹.

The simulations were performed with nondimensionalized quantities, and units of length, energy, and time were chosen at a , $k_B T$, and $\tau = \zeta a^2 / k_B T$. For star prepolymers, f and N_a were varied as $3 \leq f \leq 8$ and $N_a = 2, 5, \text{ and } 10$. The number of prepolymers, M , was chosen at 4000, 1600, and 800 for $N_a = 2, 5, \text{ and } 10$, respectively. The bead number density was fixed at 8. For the Brownian dynamics, a second-order integration scheme²² was employed, with the step size of $\Delta t = 0.01$. b_{\max}^{\square} was fixed at 2. The parameters for the end-linking reaction were chosen according to the previous studies^{15,16}; the critical distance was $r_r = 1$, and the reaction probability was $p_r = 0.1$. During the gelation, snapshots at $\varphi_c = 0.6-0.95$ were stored for stretch. The energy minimization scheme was the Broyden-Fletcher-Goldfarb-Sanno method²³. The bead displacement parameter was $\Delta r = 0.01$, and the energy conversion parameter was $\Delta u = 10^{-4}$. The magnitude of elongation at the stepwise stretch was $\Delta \varepsilon = 0.01$. b_c^{\square} was fixed at $\sqrt{1.5}$. For statistics, eight independent simulation runs were performed for each set of (f, N_a, φ_c) .

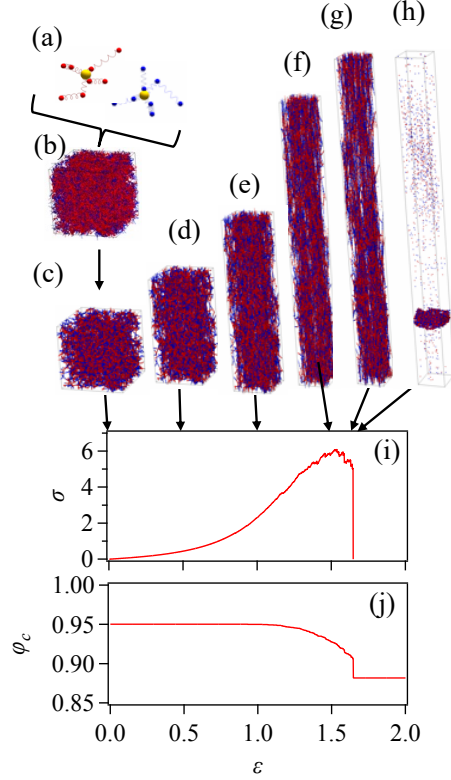


Figure 1 Typical snapshots and mechanical behavior during the simulation for $N_a = 2$ and $f = 4$ at $\varphi_c = 0.95$. Panels (a)-(c) show prepolymer and the network before and after energy-minimization. Panels (d)-(g) exhibit the network under stretch at applied true strain ε of 0.5, 1, 1.5, and 1.64, respectively. Panel (h) shows the network where the percolation was eliminated toward the elongational direction at $\varepsilon = 1.65$. The scattered dots in panel (h) are isolated fragments. Panels (i) and (j) exhibit true stress σ and conversion ratio φ_c plotted against applied strain ε .

RESULTS AND DISCUSSION

Figure 2 (a) shows the stress-strain curves obtained for $(f, \varphi_c) = (4, 0.95)$ with different N_a values. Qualitatively consistent with experiments⁶, an increase of N_a improves the mechanical properties of the network; ε_b , σ_b , and W_b increase with increasing N_a . The fracture characteristics obtained from the stress-strain curves are plotted against N_a in panels (b)-(c) for $f = 4$ and 8 (circles and triangles), and $\varphi_c = 0.6$ and 0.95 (unfilled and filled symbols). In panel (b), ε_b is converted to stretch at break $\lambda_b \equiv \exp(\varepsilon_b)$. As the red dotted line indicates, the N_a -dependence of λ_b is consistent with $N_a^{1/2}$, irrespective of f and φ_c . One may see that

fitting to $N_a^{2/3}$ suggested by Akagi et al.⁶ reasonably works as well in this plot within the error. However, $N_a^{1/2}$ is better in further assessment, as shown below. Concerning the effects of f and φ_c , λ_b (thus ε_b) decreases with increasing f and φ_c , as reported earlier⁹.

In Figs 2 (c) and (d), σ_b and W_b are shown as functions of N_a . These values also increase with increasing N_a . The N_a -dependence is a power-law manner with the exponent of 1/3, as demonstrated by dotted broken lines. σ_b and W_b increase with increasing φ_c , and the magnitude of the increase depends on f ; σ_b and W_b change significantly in small f cases. (See filled and unfilled circles that indicate the case of $f = 4$.)

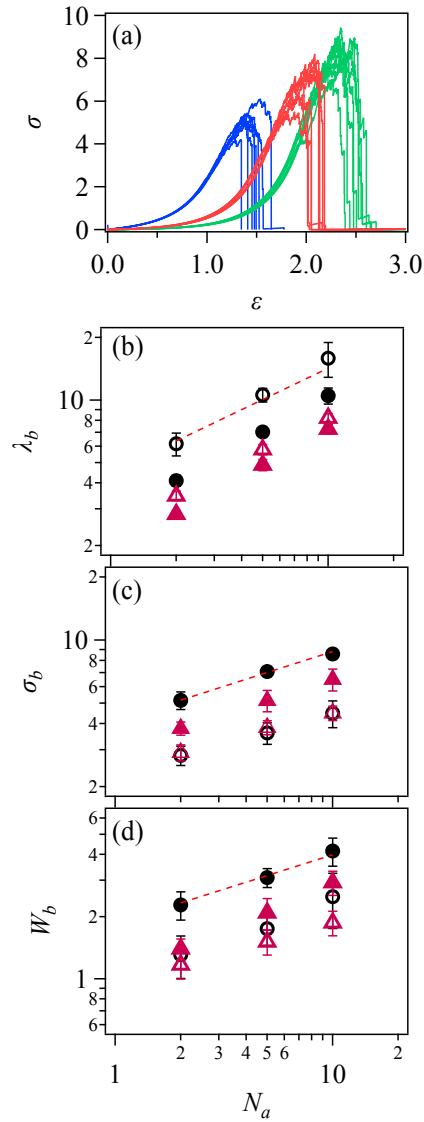
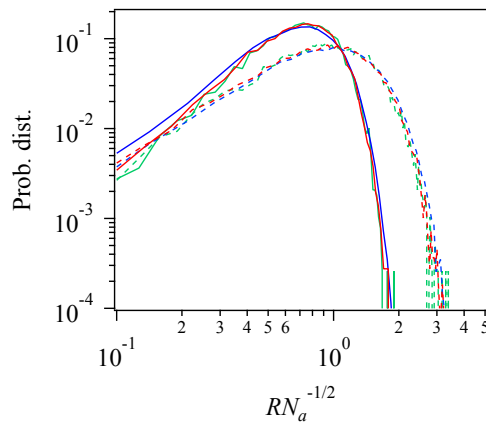


Figure 2 Typical stress-strain curves (a) and fracture characteristics extracted from the curves:

λ_b (b), σ_b (c), and W_b (d). In panel (a), the curves for $(f, \varphi_c) = (4, 0.95)$ are shown, and blue, red, and green curves are the results for $N_a = 2, 5,$ and $10,$ respectively. Eight independent simulation runs were conducted for each condition, and the curves displayed all the results. In panels (b) – (d), circles and triangles show the results of $f = 4$ and $8,$ respectively. Filled and unfilled symbols indicate the cases of $\varphi_c=0.95$ and $0.6,$ respectively. Error bars are standard deviations among eight simulation runs. Red and black broken lines in panel (b) indicate slopes of $2/3$ and $1/2,$ respectively. Red broken lines in panels (c) and (d) show a slope of $1/3.$

As discussed earlier^{2,3}, the N_a -dependence of λ_b is related to the strand length before stretch. Figure 3 (a) exhibits the strand length distribution for $f = 4,$ $\varphi_c=0.95,$ and $N_a = 2, 5,$ and 10 before and after minimization, normalized by $N_a^{1/2}.$ The strand length distribution before energy minimization (broken curves) is close to the Gaussian, and the curves overlap if normalized by $N_a^{1/2}.$ The distribution is modified by energy minimization, reflecting shrinkage of strands. See solid curves. However, even after minimization, the strand length distribution is scaled by $N_a^{1/2}.$

Figure 3 (b) shows the relation between the average strand length after energy minimization (before stretch) R_0 and $\lambda_b N_a^{-1}$ obtained for various f and φ_c values with $N_a = 2, 5,$ and $10.$ Although some downward deviations are seen for large- R_0 cases, overall, the relation $\lambda_b \sim N_a/R_0$ reasonably holds. Since Fig 3 (a) demonstrates $R_0 \sim N_a^{-1/2},$ the power-law relation between λ_b and N_a is $\lambda_b \sim N_a^{1/2},$ as discussed in Fig 2 (b).



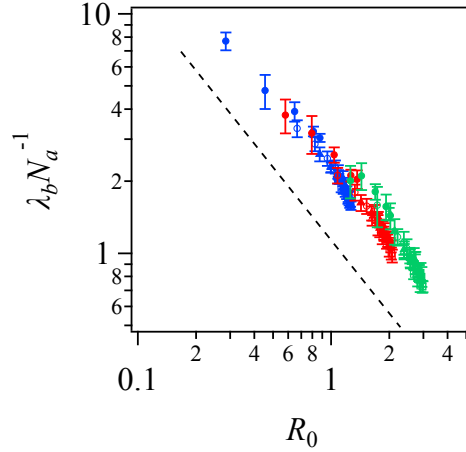


Figure 3 Strand length distribution normalized by $N_a^{-1/2}$ for $f = 4$ and $\varphi_c=0.95$ (a) and the relation between average strand length after energy minimization R_0 and $\lambda_b N_a^{-1}$ for various f and φ_c (b). The results for $N_a = 2, 5,$ and 10 are indicated in blue, red, and green, respectively. In panel (a), broken and solid curves correspond to structures before and after energy minimization. In panel (b), error bars exhibit standard deviations among eight independent simulation runs, and the broken line shows a slope of -1 .

For further discussion, the fracture characteristics concerning the cycle rank of the network are analyzed according to the earlier studies⁹⁻¹³. Figure 4 shows cycle rank ξ , the number of closed loops per branch point in the percolated network. Irrespective of N_a , ξ is consistent with the mean-field theory²⁴⁻²⁶. This consistency means that the end-linking reactions simulated in the gelation process are independent, and the formation of second and higher-order loops is negligible. (Note that primary loops are not created by construction.) The consistency also demonstrates that the examined networks are stochastically random regarding network connectivity.

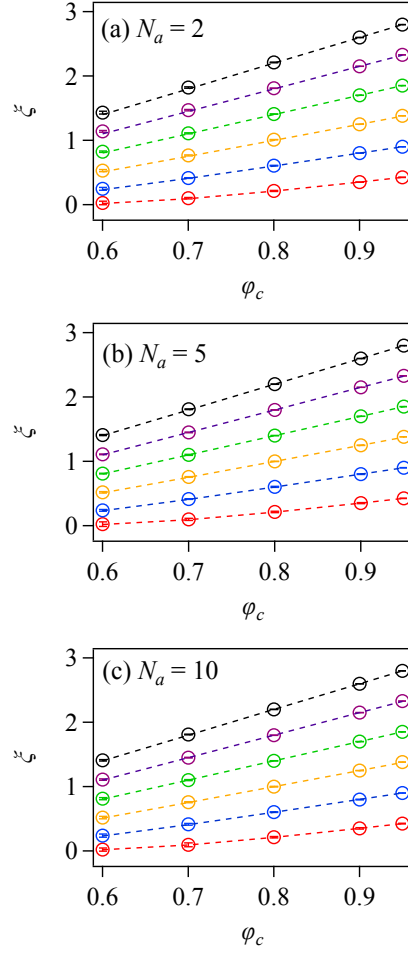


Figure 4 Cycle rank ξ plotted against φ_c for various f with $N_a=2$ (a), 5 (b), and 10 (c). The simulation results for $f=3, 4, 5, 6, 7,$ and 8 , are shown by circles in red, blue, orange, green, violet, and black, respectively. The broken curves illustrate the mean-field theory. Although standard deviations among eight different simulation runs are shown by error bars, they are smaller than the symbol. The results for $N_a = 5$ (panel (b)) are identical to what has been presented earlier.

According to the phantom network theory²⁷, cycle rank ξ dominates modulus G . This argument is examined in Fig. 5, where G normalized by the branch point density $v_{br} \equiv \rho/(fN_a + 1)$ is shown as a function of ξ . Here, G was obtained from stress-strain curves as $G = \sigma(\lambda^2 - \lambda^{-1})$ at $\lambda^{-1} = 0.75$, according to the previous studies. Gv_{br}^{-1} obtained for various f , φ_c , and N_a values are located on a single master curve, with a weak non-linearity in the small ξ region. As discussed previously¹³, the observed non-linearity and non-universality are due to inert segments,

such as dangling domains that are included in the percolated network but do not sustain stress. Indeed, Gv_{br}^{-1} is proportional to ξ_{eff} , which is cycle rank obtained only for effective strands carrying stress, as demonstrated previously¹³.

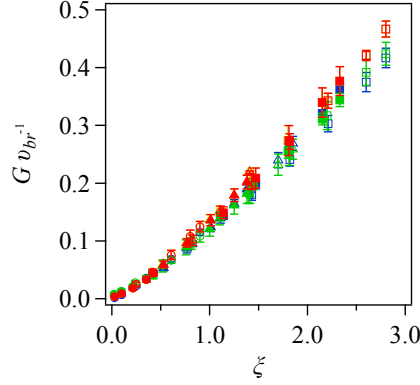


Figure 5 Modulus G normalized by the branch point density v_{br} plotted against cycle rank ξ for various f , φ_c , and N_a values. The results for $N_a=2, 5$, and 10 are colored in blue, red, and green, respectively. Symbols indicate $f = 3$ (filled circle), 4 (unfilled circle), 5 (filled triangle), 6 (unfilled triangle), 7 (filled square), and 8 (unfilled square). Error bars correspond to the standard deviations for eight different simulation runs for each condition.

Figure 6 (a) exhibits strain at break ε_b plotted against ξ for various f , φ_c , and N_a values. ε_b obtained for different f and φ_c values lie on a master curve for each N_a , and the curve depends on N_a ; ε_b increases with increasing N_a . Fig 6 (b) shows $\lambda_b N_a^{-1/2}$, demonstrating overlapping among curves for different N_a values and rationalizing the relation $\lambda_b \sim N_a^{1/2}$. The inset demonstrates that $\lambda_b N_a^{-1/2}$ decays in a power-law manner with increasing ξ , and the power-law exponent is close to $-1/3$ shown by the red line in the inset. Figure 6 (c) displays the average strand length before stretch (after energy minimization) R_0 normalized by $N_a^{1/2}$ owing to its distribution shown in Fig 3. Consistent with $\lambda_b N_a^{-1/2}$, $R_0 N_a^{-1/2}$ data obtained for various f , φ_c , and N_a values draws a master curve. The ξ -dependence of $R_0 N_a^{-1/2}$ is not power-law-like but upper-limited by a specific value for $\xi \rightarrow \infty$.

It so appears that λ_b depends on $N_a^{1/2}$ rather than $N_a^{2/3}$. The reasons for this discrepancy are explained as follows. The primary reason is the difference in the network structure before the stretch. The examined networks in this study consist of phantom chains without specific

interactions between segments, whereas in the experimentally investigated gels^{6,8}, osmotic and excluded volume interactions play significant roles. Another possible reason is the difference between the stretch at break and the maximum stretch parameter in the stress-strain relation; the former is induced by breakage of a specific strand followed by cascade scission of other strands, whereas the latter reflects segment stretch on average. These two parameters coincide when all the strands are equally stretched and are not necessarily the same for other cases.

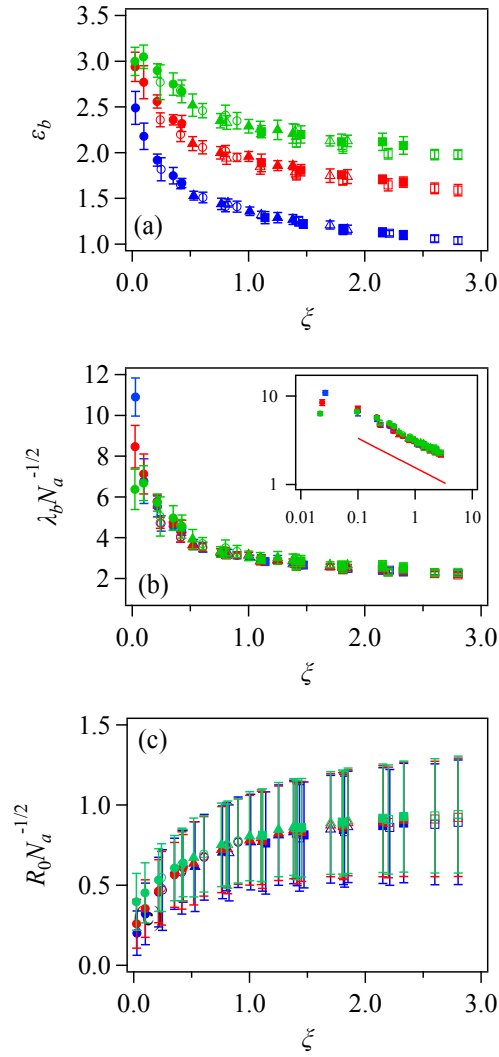


Figure 6 Strain at break ϵ_b (a), stretch at break $\lambda_b = \exp(\epsilon_b)$ (b), and average minimized strand length before stretch R_0 (c) plotted against cycle rank ξ for the examined networks with various f and φ_c values. λ_b and R_0 are normalized by $N_a^{1/2}$. The results for $N_a=2, 5$, and 10, are colored in blue, red, and green, respectively. Symbols indicate $f = 3$ (filled circle), 4

(unfilled circle), 5 (filled triangle), 6 (unfilled triangle), 7 (filled square), and 8 (unfilled square). Error bars correspond to the standard deviations for eight different simulation runs for each condition. The inset in Panel (b) shows the logarithmic plot, in which the red solid line exhibits a slope of $-1/3$.

Let us turn our attention to the other fracture characteristics rather than λ_b . Figure 7 (a) shows stress at break σ_b plotted against ξ . Differently from ε_b , this plot exhibits a scattering of the data. As demonstrated previously^{10,13}, σ_b data for various f and φ_c lie on a master curve if normalized by the number density of branch point $v_{br} \equiv \rho/(fN_a + 1)$ for each N_a , as shown in Panel (b). $\sigma_b v_{br}^{-1}$ increases with increasing N_a because $\sigma_b \propto N_a^{1/3}$ (see Fig 2(c)) and $v_{br} \sim N_a^{-1}$. Thus, N_a -dependence is expected as $\sigma_b v_{br}^{-1} \propto N_a^{4/3}$. Indeed, panel (c) demonstrates that all the curves converge by the normalization by $N_a^{4/3}$. The inset shows the logarithmic plot, implying a power-law relation $\sigma_b v_{br}^{-1} N_a^{-4/3} \propto \xi^{1/3}$.

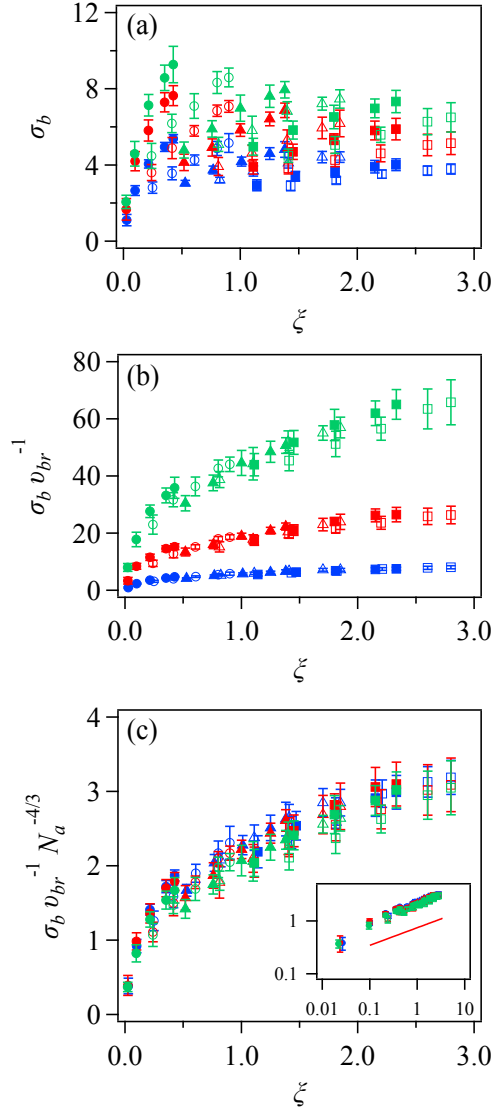


Figure 7 Stress at break σ_b (a), σ_b normalized by the branch point density v_{br} (b), σ_b normalized by $v_{br}N_a^{4/3}$ (c), plotted against cycle rank ξ for the examined networks with various f and φ_c values. The results for $N_a = 2, 5,$ and 10 , are colored in blue, red, and green, respectively. Symbols indicate $f = 3$ (filled circle), 4 (unfilled circle), 5 (filled triangle), 6 (unfilled triangle), 7 (filled square), and 8 (unfilled square). Error bars correspond to the standard deviations for eight different simulation runs for each condition. The inset in Panel (b) shows the logarithmic plot, in which the red solid line exhibits a slope of $1/3$.

Figure 8 shows work for fracture W_b . As seen for σ_b , the plot of W_b against ξ in panel (a) exhibits no systematic behavior. As previously reported^{10,13}, a master curve appears when W_b is

normalized by v_{br} as shown in panel (b). The curve depends on N_a similarly to that for σ_b ; $W_b v_{br}^{-1}$ increases with increasing N_a . This N_a -dependence can be accommodated by the normalization with $N_a^{4/3}$ as seen in panel (c). The final master curve shows a power-law relation $W_b v_{br}^{-1} N_a^{-4/3} \propto \xi^{1/3}$.

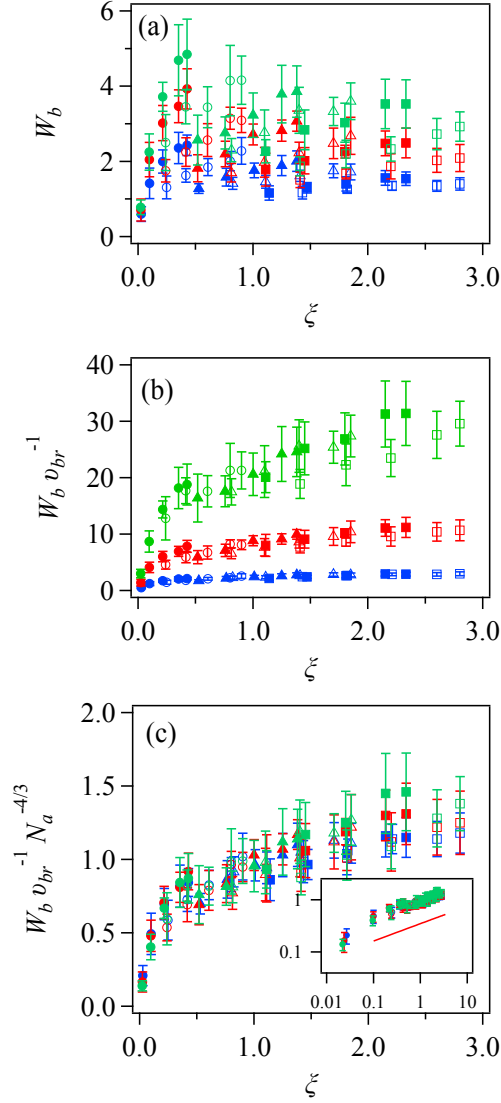


Figure 8 Work for fracture W_b (a), W_b normalized by the branch point density v_{br} (b), W_b normalized by $v_{br} N_a^{4/3}$ (c), plotted against cycle rank ξ for the examined networks with various f and φ_c values. The results for $N_a = 2, 5$, and 10 , are colored in blue, red, and green, respectively. Symbols indicate $f = 3$ (filled circle), 4 (unfilled circle), 5 (filled triangle), 6 (unfilled triangle), 7 (filled square), and 8 (unfilled square). Error bars correspond to the standard deviations for eight different simulation runs for each condition. The inset in Panel (b) shows the

logarithmic plot, in which the red solid line exhibits a slope of 1/3.

The previous studies⁹⁻¹¹ demonstrated that the number fraction of broken strands φ_{bb} exhibits similar ξ -dependence to σ_b and W_b , as shown in Fig 9. Panels (a) (b) and (c) display φ_{bb} , $\varphi_{bb}v_{br}^{-1}$, and $\varphi_{bb}v_{br}^{-1}N_a^{-4/3}$ plotted against ξ . φ_{bb} is scattered if plotted against ξ , whereas $\varphi_{bb}v_{br}^{-1}$ lie on master curves depending on N_a . The N_a -dependence of the master curve is newly reported in the present study. The normalization by $N_a^{4/3}$ is attempted in Panel (c). The logarithmic plot in the inset implies a power-law relation $\varphi_{bb}v_{br}^{-1}N_a^{-4/3} \propto \xi^{2/3}$. Note that the power-law exponent is 2/3, larger than 1/3 for σ_b and W_b in Figs 5 and 6.

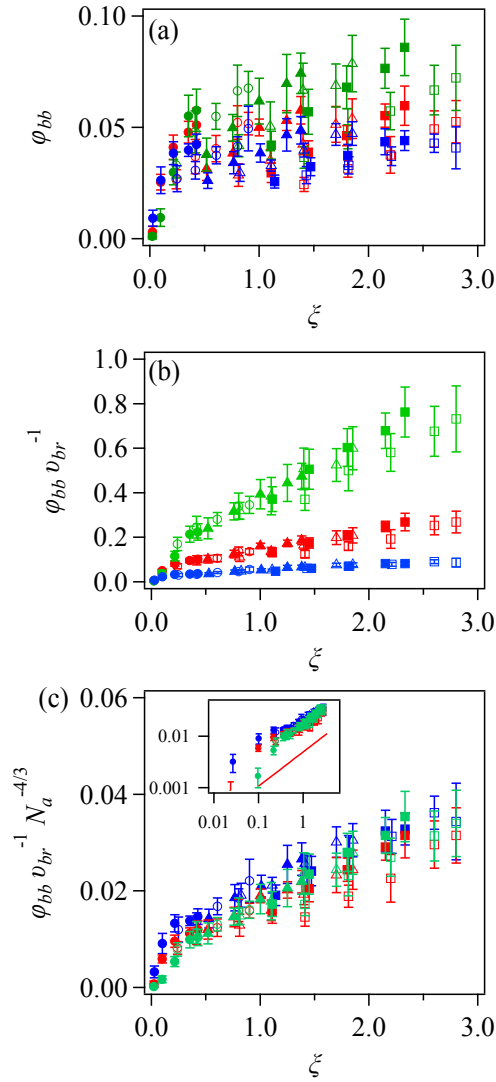


Figure 9 Broken bond fraction φ_{bb} (a), φ_{bb} normalized by the branch point density v_{br} (b),

φ_{bb} normalized by $v_{br}N_a^{4/3}$ (c), plotted against cycle rank ξ for the examined networks with various f and φ_c values. The results for $N_a = 2, 5,$ and 10 , are colored in blue, red, and green, respectively. Symbols indicate $f = 3$ (filled circle), 4 (unfilled circle), 5 (filled triangle), 6 (unfilled triangle), 7 (filled square), and 8 (unfilled square). Error bars correspond to the standard deviations for eight different simulation runs for each condition. The inset in Panel (b) shows the logarithmic plot, in which the red solid line exhibits a slope of $2/3$.

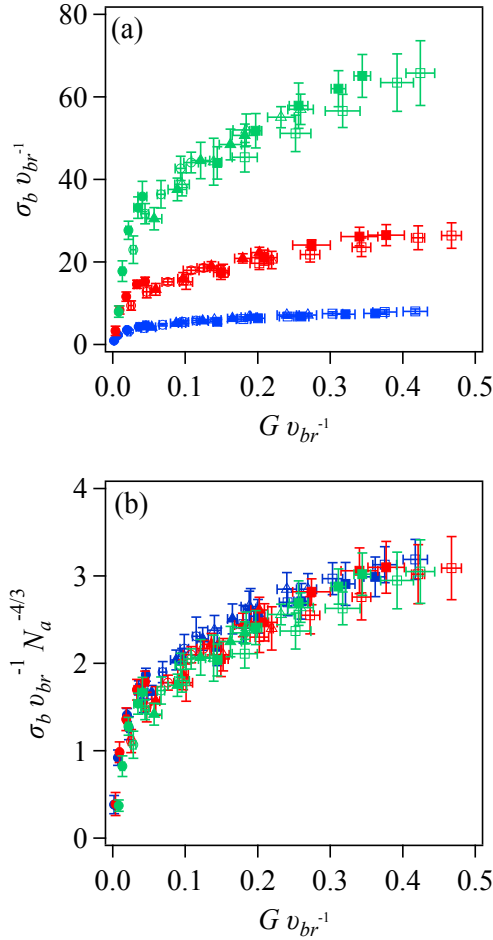


Figure 10 Relation between stress at break σ_b and modulus G , both normalized by v_{br}^{-1} in panel (a) and by $v_{br}^{-1}N_a^{-4/3}$ for σ_b in panel (b). The results for $N_a = 2, 5,$ and 10 , are colored in blue, red, and green, respectively. Symbols indicate $f = 3$ (filled circle), 4 (unfilled circle), 5 (filled triangle), 6 (unfilled triangle), 7 (filled square), and 8 (unfilled square). Error bars correspond to the standard deviations for eight different simulation runs for each condition.

According to the Lake-Thomas theory²⁸, fracture energy is often discussed in tearing tests as related to modulus²⁹⁻³¹. Although the network rupture examined in this study cannot be directly compared with fracture under tearing, modulus reflects the effective cycle rank as discussed in Fig 5; thus, the relation between modulus and fracture characteristics is worth examining. In this regard, the relation between stress at break σ_b and modulus G is explored in Fig 10. Panel (a) demonstrates that σ_b is a single-value function of G if both are normalized by the branch point density ν_{br} . However, the curve depends on N_a , and consequently, σ_b is not determined by G . Since the N_a -dependence of $\sigma_b \nu_{br}^{-1}$ can be accommodated by the normalization by $N_a^{4/3}$, panel (b) exhibits $\sigma_b \nu_{br}^{-1} N_a^{-4/3}$ plotted against $G \nu_{br}^{-1}$. The curves come close to each other, and a master curve appears. Similar master curves can be obtained between the other quantities.

CONCLUSIONS

By phantom chain network simulations, the effects of prepolymer arm molecular weight N_a for star polymer networks on the fracture under stretch were investigated. From the stress-strain curves for the networks with various node functionalities f and conversion ratios φ_c , strain and stress at break, ε_b and σ_b , and work for fracture W_b , were collected. ε_b (and thus $\lambda_b = \exp(\varepsilon_b)$) draw master curves if plotted against the cycle rank of the percolated network ξ , in which the effects of f and φ_c are embedded. The master curve depends on N_a , and the N_a -dependence can be accommodated by normalization according to $N_a^{1/2}$, consistent with the fact that the strand length distribution before stretch is universal under normalization by $N_a^{1/2}$. For σ_b and W_b , they also lie on master curves against ξ if normalized by the branch point density ν_{br} . Although the curves depend on N_a , further normalization by $N_a^{4/3}$ attains super master curves. The ξ -dependence for each fracture characteristic is described by a power-law function, although there is no theoretical basis at preset. The resultant relations are summarized as follows: $\lambda_b \sim N_a^{1/2} \xi^{-1/3}$, $\sigma_b \sim \nu_{br} N_a^{4/3} \xi^{2/3}$, and $W_b \sim \nu_{br} N_a^{4/3} \xi^{2/3}$.

Since the abovementioned relations between fracture characteristics and the structural parameters are reported for the first time for phantom chain networks, they would give a basis for summarizing the data. However, it should be emphasized that there is no theory for the proposed functional forms, and they are not more than eye-guides at this time. Although the significance of cycle rank is obvious, other structural parameters like minimum path length^{4,5}, loop density^{32,33},

loop length^{29,34}, etc., may be better to construct theoretical models. It should also be noted that the reported results are for energy-minimized phantom chain networks. Thus, the results may vary if one considers Brownian motion, osmotic force, excluded volume interactions and entanglements, etc. Subsequent studies in such directions are ongoing, and the results will be reported elsewhere.

ACKNOWLEDGEMENTS

This study is partly supported by JST-CREST (JPMJCR1992) and JSPS KAKENHI (22H01189).

References

- (1) Sakai, Takamasa. *Physics of Polymer Gels*; Sakai, T., Ed.; Wiley, 2020.
<https://doi.org/10.1002/9783527346547>.
- (2) Kuhn, W. Dependence of the Average Transversal on the Longitudinal Dimensions of Statistical Coils Formed by Chain Molecules. *Journal of Polymer Science* **1946**, *1* (5), 380–388. <https://doi.org/10.1002/pol.1946.120010505>.
- (3) Obukhov, S. P.; Rubinstein, M.; Colby, R. H. *Network Modulus and Superelasticity*, 1994; Vol. 27. <https://pubs.acs.org/sharingguidelines>.
- (4) Stevens, M. J. Interfacial Fracture between Highly Cross-Linked Polymer Networks and a Solid Surface: Effect of Interfacial Bond Density. *Macromolecules* **2001**, *34* (8), 2710–2718. <https://doi.org/10.1021/ma000553u>.
- (5) Lin, S.; Ni, J.; Zheng, D.; Zhao, X. Fracture and Fatigue of Ideal Polymer Networks. *Extreme Mech Lett* **2021**, *48*.
<https://doi.org/10.1016/j.eml.2021.101399>.
- (6) Akagi, Y.; Katashima, T.; Sakurai, H.; Chung, U. Il; Sakai, T. Ultimate Elongation of Polymer Gels with Controlled Network Structure. *RSC Adv* **2013**, *3* (32), 13251–13258. <https://doi.org/10.1039/c3ra41580e>.
- (7) Katashima, T.; Asai, M.; Urayama, K.; Chung, U. Il; Sakai, T. Mechanical Properties of Tetra-PEG Gels with Supercoiled Network Structure. *Journal of Chemical Physics* **2014**, *140* (7). <https://doi.org/10.1063/1.4863917>.

- (8) Fujiyabu, T.; Sakumichi, N.; Katashima, T.; Liu, C.; Mayumi, K.; Chung, U.; Sakai, T. Tri-Branched Gels: Rubbery Materials with the Lowest Branching Factor Approach the Ideal Elastic Limit. *Sci Adv* **2022**, *8* (14), abk0010_1-abk0010_10. <https://doi.org/10.1126/sciadv.abk0010>.
- (9) Masubuchi, Y.; Doi, Y.; Ishida, T.; Sakumichi, N.; Sakai, T.; Mayumi, K.; Satoh, K.; Uneyama, T. Phantom-Chain Simulations for the Effect of Node Functionality on the Fracture of Star-Polymer Networks. *Macromolecules* **2023**, *56* (23), 9359–9367. <https://doi.org/10.1021/acs.macromol.3c01291>.
- (10) Masubuchi, Y. Phantom Chain Simulations for Fracture of End-Linking Networks. *Polymer (Guildf)* **2024**, *297*, 126880. <https://doi.org/10.1016/j.polymer.2024.126880>.
- (11) Masubuchi, Y. Phantom Chain Simulations for Fracture of Polymer Networks Created from Star Polymer Mixtures of Different Functionalities. *Polym J* **2024**, *56* (3), 163–171. <https://doi.org/10.1038/s41428-023-00862-w>.
- (12) Masubuchi, Y. Phantom Chain Simulations for the Effect of Stoichiometry on the Fracture of Star-Polymer Networks. *Nihon Reoroji Gakkaishi* **2024**, *52* (1), 21–26. <https://doi.org/10.1678/rheology.52.21>.
- (13) Masubuchi, Y.; Ishida, T.; Koide, Y.; Uneyama, T. Phantom Chain Simulations for the Fracture of Star Polymer Networks with Various Strand Densities. *Soft Matter* **2024**. <https://doi.org/10.1039/D4SM00726C>.
- (14) Masubuchi, Y.; Doi, Y.; Ishida, T.; Sakumichi, N.; Sakai, T.; Mayumi, K.; Uneyama, T. Phantom Chain Simulations for the Fracture of Energy-Minimized Tetra- and Tri-Branched Networks. *Macromolecules* **2023**, *56* (5), 2217–2223. <https://doi.org/10.1021/acs.macromol.3c00047>.
- (15) Masubuchi, Y.; Uneyama, T. Retardation of the Reaction Kinetics of Polymers Due to Entanglement in the Post-Gel Stage in Multi-Chain Slip-Spring Simulations. *Soft Matter* **2019**, *15*, 5109–5115. <https://doi.org/10.1039/C9SM00681H>.
- (16) Masubuchi, Y.; Yamazaki, R.; Doi, Y.; Uneyama, T.; Sakumichi, N.; Sakai, T. Brownian Simulations for Tetra-Gel-Type Phantom Networks Composed of

- Prepolymers with Bidisperse Arm Length. *Soft Matter* **2022**, *18*, 4715–4724.
<https://doi.org/10.1039/d2sm00488g>.
- (17) Lang, M. On the Elasticity of Polymer Model Networks Containing Finite Loops. *Macromolecules* **2019**, *52* (16), 6266–6273.
<https://doi.org/10.1021/acs.macromol.9b00996>.
- (18) Nishi, K.; Noguchi, H.; Sakai, T.; Shibayama, M. Rubber Elasticity for Percolation Network Consisting of Gaussian Chains. *J Chem Phys* **2015**, *143* (18), 184905.
<https://doi.org/10.1063/1.4935395>.
- (19) Nishi, K.; Chijiishi, M.; Katsumoto, Y.; Nakao, T.; Fujii, K.; Chung, U.; Noguchi, H.; Sakai, T.; Shibayama, M. Rubber Elasticity for Incomplete Polymer Networks. *J Chem Phys* **2012**, *137* (22), 224903. <https://doi.org/10.1063/1.4769829>.
- (20) Lei, J.; Li, Z.; Xu, S.; Liu, Z. A Mesoscopic Network Mechanics Method to Reproduce the Large Deformation and Fracture Process of Cross-Linked Elastomers. *J Mech Phys Solids* **2021**, *156* (August), 104599.
<https://doi.org/10.1016/j.jmps.2021.104599>.
- (21) Arora, A.; Lin, T. S.; Olsen, B. D. Coarse-Grained Simulations for Fracture of Polymer Networks: Stress Versus Topological Inhomogeneities. *Macromolecules* **2022**, *55* (1), 4–14. <https://doi.org/10.1021/acs.macromol.1c01689>.
- (22) Honeycutt, R. L. Stochastic Runge-Kutta Algorithms. I. White Noise. *Phys Rev A (Coll Park)* **1992**, *45* (2), 600–603.
<https://doi.org/10.1103/PhysRevA.45.600>.
- (23) Nocedal, J. Updating Quasi-Newton Matrices with Limited Storage. *Math Comput* **1980**, *35* (151), 773. <https://doi.org/10.2307/2006193>.
- (24) Macosko, C. W.; Miller, D. R. A New Derivation of Average Molecular Weights of Nonlinear Polymers. *Macromolecules* **1976**, *9* (2), 199–206.
<https://doi.org/10.1021/ma60050a003>.
- (25) Macosko, C. W.; Miller, D. R. Calculation of Average Molecular Properties during Nonlinear, Living Copolymerization. *Makromol. Chem.* **1991**, *192*, 377–404.
- (26) Yoshikawa, Y.; Sakumichi, N.; Chung, U.; Sakai, T. Connectivity Dependence of

- Gelation and Elasticity in AB-Type Polymerization: An Experimental Comparison of the Dynamic Process and Stoichiometrically Imbalanced Mixing. *Soft Matter* **2019**, *15* (25), 5017–5025. <https://doi.org/10.1039/c9sm00696f>.
- (27) James, H. M.; Guth, E. Theory of the Elastic Properties of Rubber. *J Chem Phys* **1943**, *11* (10), 455–481. <https://doi.org/10.1063/1.1723785>.
- (28) Lake, J.; Thomas, A. G. The Strength of Highly Elastic Materials. *Proc R Soc Lond A Math Phys Sci* **1967**, *300* (1460), 108–119. <https://doi.org/10.1098/rspa.1967.0160>.
- (29) Wang, S.; Panyukov, S.; Rubinstein, M.; Craig, S. L. Quantitative Adjustment to the Molecular Energy Parameter in the Lake-Thomas Theory of Polymer Fracture Energy. *Macromolecules* **2019**, *52* (7), 2772–2777. <https://doi.org/10.1021/acs.macromol.8b02341>.
- (30) Barney, C. W.; Ye, Z.; Sacligil, I.; McLeod, K. R.; Zhang, H.; Tew, G. N.; Riggleman, R. A.; Crosby, A. J. Fracture of Model End-Linked Networks. *Proceedings of the National Academy of Sciences* **2022**, *119* (7), 2–7. <https://doi.org/10.1073/pnas.2112389119>.
- (31) Akagi, Y.; Sakurai, H.; Gong, J. P.; Chung, U.; Sakai, T. Fracture Energy of Polymer Gels with Controlled Network Structures. *J Chem Phys* **2013**, *139* (14). <https://doi.org/10.1063/1.4823834>.
- (32) Zhong, M.; Wang, R.; Kawamoto, K.; Olsen, B. D.; Johnson, J. A. Quantifying the Impact of Molecular Defects on Polymer Network Elasticity. *Science (1979)* **2016**, *353* (6305), 1264–1268. <https://doi.org/10.1126/science.aag0184>.
- (33) Lin, S.; Zhao, X. Fracture of Polymer Networks with Diverse Topological Defects. *Phys Rev E* **2020**, *102* (5), 52503. <https://doi.org/10.1103/PhysRevE.102.052503>.
- (34) Wang, S.; Panyukov, S.; Craig, S. L.; Rubinstein, M. Contribution of Unbroken Strands to the Fracture of Polymer Networks. *Macromolecules* **2023**, *56* (6), 2309–2318. <https://doi.org/10.1021/acs.macromol.2c02139>.